Delft University of Technology

Experimentally validated meso-scale fracture modelling of mortar using output from micromechanical models

Zhang, Hongzhi; Xu, Yading; Gan, Yidong; Schlangen, Erik; Šavija, Branko

DOI
10.1016/j.cemconcomp.2020.103567

Publication date
2020

Document Version
Final published version

Published in
Cement and Concrete Composites

Citation (APA)
Zhang, H., Xu, Y., Gan, Y., Schlangen, E., & Šavija, B. (2020). Experimentally validated meso-scale fracture modelling of mortar using output from micromechanical models. *Cement and Concrete Composites*, *110*, 1-12. Article 103567. https://doi.org/10.1016/j.cemconcomp.2020.103567

Important note
To cite this publication, please use the final published version (if applicable).
Please check the document version above.

Copyright
Other than for strictly personal use, it is not permitted to download, forward or distribute the text or part of it, without the consent of the author(s) and/or copyright holder(s), unless the work is under an open content license such as Creative Commons.

Takedown policy
Please contact us and provide details if you believe this document breaches copyrights.
We will remove access to the work immediately and investigate your claim.

This work is downloaded from Delft University of Technology.
For technical reasons the number of authors shown on this cover page is limited to a maximum of 10.

Cement and Concrete Composites 110 (2020) 103567

Contents lists available at ScienceDirect

Cement and Concrete Composites

journal homepage: http://www.elsevier.com/locate/cemconcomp

Experimentally validated meso-scale fracture modelling of mortar using output from micromechanical models

Hongzhi Zhang [a,b], Yading Xu [a,*], Yidong Gan [a], Erik Schlangen [a], Branko Šavija [a]

[a] Faculty of Civil Engineering and Geosciences, Delft University of Technology, 2628 CN, Delft, the Netherlands
[b] School of Qilu Transportation, Shandong University, 250002, Jinan, PR China

ARTICLE INFO

Keywords:
Mortar
Fracture behaviour
Multi-scale modelling scheme
Discrete lattice model

ABSTRACT

This paper presents a validation process of the developed multi-scale modelling scheme on mortar composites. Special attention was paid to make the material structure of real and virtual mortar specimens comparable at the meso-scale. The input mechanical parameters of cement paste (both bulk cement paste and interfacial transition zone) at the meso-scale were derived from results of micromechanical modelling through a volume averaging approach. Two constitutive relations for local elements were assumed and tested. By comparing with the experiments, the model using linear-elastic constitutive relation showed to be capable to reproduce the experimental load-displacement response satisfactorily in terms of the elastic stage and peak load. However, in the non-elastic stage a more realistic load-displacement curve can be simulated by considering the softening of cement paste using a step-wise approach. More importantly, the proposed multi-scale modelling scheme is validated by the experimental measurements. The proposed development offers the opportunity for the meso-scale model to become fully predictive.

1. Introduction

Cementitious materials are heterogeneous at multiple length scales, ranging from nanometres to millimetres [1]. In light of its multi-scale nature [2–11], the behaviour of cementitious materials and structures can be analysed at several different length scales: nano-scale, sub--micro-scale, micro-scale, meso-scale and macro-scale. The nano-scale deals with atomic nature of concrete, while the sub-nano-scale is introduced to accounts for colloidal and gel-like properties of calcium-silicate-hydrate. At micro-scale, the internal structure of hardened cement paste is the most important structural feature, comprising various phases such as anhydrous cement particles, capillary pores and hydration products. The meso-scale deals with structures consisting of cement matrix, aggregates with different particle sizes and air voids. At macro-scale, no internal material structure is recognised, and concrete is considered as a homogeneous, isotropic continuum.

Numerous efforts have been made for modelling the fracture behaviour of cementitious materials on the meso-scale. In general, fracture of concrete on the meso-scale is modelled using discrete models [12–20] or finite element models [21–29]. Overall, while this can be done in a qualitative sense, quantitative prediction in terms of the crack pattern and stress-strain response is still a challenging task. This is partly because of the complex material structure: between aggregate and cement paste matrix, there exists a so-called interfacial transition zone (ITZ). This zone is a highly porous region of cement paste surrounding aggregate particles. With a thickness reported to range between 30 and 80 μm, the ITZ is generally considered to be the weakest part of the cementitious composite [30–34]. Therefore, a large number of micro-cracks form in this zone when concrete is loaded before crack coalescence and localization. However, explicitly representation of this zone in a meso-scale model is computationally expensive. Consequently, most studies that do are limited to two dimensions, and cannot capture formation of non-planar 3D fracture surfaces. Several attempts have been made to simulate fracture of cementitious materials on the meso-scale in three-dimensions, using discrete models [19,20,35–38] and finite elements models [25,39–46]. However, in all these publications a rather coarse mesh is used to discretize the system. Moreover, input parameters in these models are commonly obtained through inverse analysis, which decreases the predictive capabilities of such models.

From a multi-scale point of view, the constitutive relation of the cement matrix and the ITZ should be preferably derived from lower-

* Corresponding author.
E-mail addresses: hzzhang@sdu.edu.cn (H. Zhang), Y.Xu-5@tudelft.nl (Y. Xu), Y.Gan@tudelft.nl (Y. Gan), erik.schlangen@tudelft.nl (E. Schlangen), b.savija@tudelft.nl (B. Šavija).

https://doi.org/10.1016/j.cemconcomp.2020.103567
Received 17 September 2019; Received in revised form 16 January 2020; Accepted 18 February 2020
Available online 22 February 2020
0958-9465/© 2020 The Authors. Published by Elsevier Ltd. This is an open access article under the CC BY-NC-ND license (http://creativecommons.org/licenses/by-nc-nd/4.0/).

scale (i.e. micro-scale) simulations or measurements. However, direct mechanical testing of cementitious materials on the micro-scale is still rare, and micromechanical properties are usually determined by simulations [3,5,47–50]. More importantly, the properties are significantly different depending on the model used. Therefore, these predicted micromechanical properties cannot be reliably used as input for the meso-scale modelling. Recently, the authors have successfully prepared and tested the micro-scale sized specimens using a micro-dicing saw (commonly used for cutting silicon wafers) and a nanoindenter [51–53]. Based on the experimental measurements, micromechanical models for both bulk cement pate and ITZ have been calibrated and validated under different loading conditions [51,52,54]. Such models can provide reliable results which can be used as input for modelling concrete fracture on the meso-scale. However, before this can be done, micromechanical properties must be upscaled. Either a concurrent [55,56] or a hierarchical [3–5] upscaling scheme is commonly used. In terms of the hierarchical scheme, an uncoupled averaging volume approach, in which the simulated global mechanical responses at the finer scale are assigned as local mechanical properties on the higher scale has been commonly adopted. This up-scaling approach has been validated in a cement paste system by the authors [57,58]. However, when dealing with mortar or concrete, the modelling scheme is further complicated by the presence of ITZ. Thus, the approach should be validated at the meso-scale considering a composite comprising the aggregate, ITZ and the cement matrix.

To this end, a comparison between experimental test and numerical modelling is carefully designed in this work. To avoid the influence of size effect in cementitious materials [59,60], the material volume in the model and the test must are taken to be identical. As a compromise between computational efficiency and experimental possibilities, the sample size is set as 10 mm herein. To consider realistic particle shapes in the model, sand aggregates with realistic shape were modelled and packed using a so-called Anm particle packing model [61]. The Delft discrete lattice model was used to model the fracture process. For the ITZ and the cement matrix, constitutive relations are derived from the results of micromechanical modelling presented in the authors' previous work [54,62], while strain-softening is implemented to consider the influence of heterogeneity which occurs at the micro-scale but is not explicitly modelled at the meso-scale. On the other hand, aggregate particles are simulated as linear-elastic/perfectly brittle. This approach should allow quantitative prediction without further calibration of input parameters at the meso-scale. A uniaxial tension test was conducted on both the real and the virtual specimens. A reasonable agreement between the simulation and the experiments was found, which shows the feasibility of using the volume averaging approach to link the micro-scale and the meso-scale. Together with the work presented previously by the authors [51,54,57,58,63], an experimentally validated multi-scale modelling framework with fully predictive capabilities at the meso-scale is devised.

2. Experimental

2.1. Materials and sample preparation

The mortar mixture was prepared using standard CEM I 42.5 N Portland cement, deionized water and crushed quartzite sand with a particle size between 1 mm and 2 mm. The specimens were prepared with a water to cement (w/c) ratio of 0.3 and sand was added at 70% of cement mass. The amount of sand and its particle size is selected to be identical as the aggregate particle size in the numerical model, making comparison easier. First, sand was mixed with dry cement in a bowl for 30 s using a Hobart mixer. Then, deionized water was added within 10 s. This was followed by mixing for 90 s at low speed. The mixer was then stopped for 30 s during which paste adhering to the walls and the bottom of the bowl was scrapped off using a metal scraper and added to the mixture. The mixing was then resumed for additional 90 s. The total mixing time was around 3 min. After mixing, the fresh mixture was cast in a cylindrical mould (24 mm diameter, 39 mm height) and vibrated for 30 s to minimize the amount of entrapped air. The cylinders were then sealed and cured for 28 days at lab conditions (temperature: 22 ± 2 °C). After curing, cubic specimens with size of 10 mm (Fig. 1) were sawn out from the cylinders. Two notches (1 mm depth and 1 mm thick) were sawn in at mid-height, see Fig. 1.

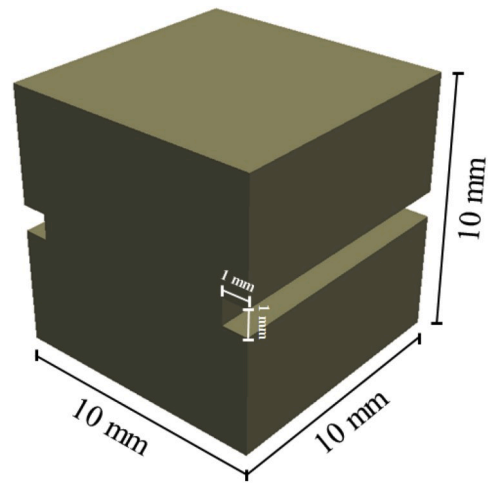

Fig. 1. Dimensions of the prepared mortar specimen for the uniaxial tension test.

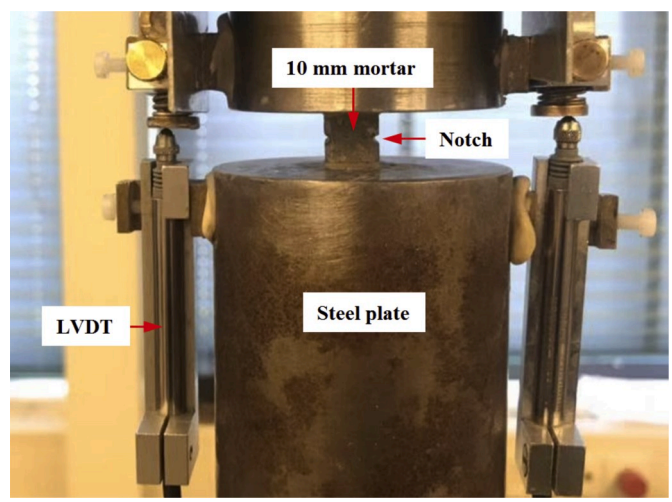

Fig. 2. Configuration of the uniaxial tension test of the 10 mm mortar.

2.2. Uniaxial tension test

For the uniaxial tension test, an Instron 8872 loading device was used. The test configuration is shown in Fig. 2. A two-component glue (X60 consisting of a power Plex 7742 and a fluid Pleximon 801) was used to bind the 10 mm mortar with the two fixed steel plates. The displacement between the two steel plates was measured continuously by two linear variable differential transformers (LVDT) at the notched sides. A constant loading speed of 15 nm/s was used, which was controlled by the average of the two LVDT's.

3. Geometrical models

The composite geometrical structure of mortar was represented by a model consisting of sand, entrapped air voids and cement paste matrix at

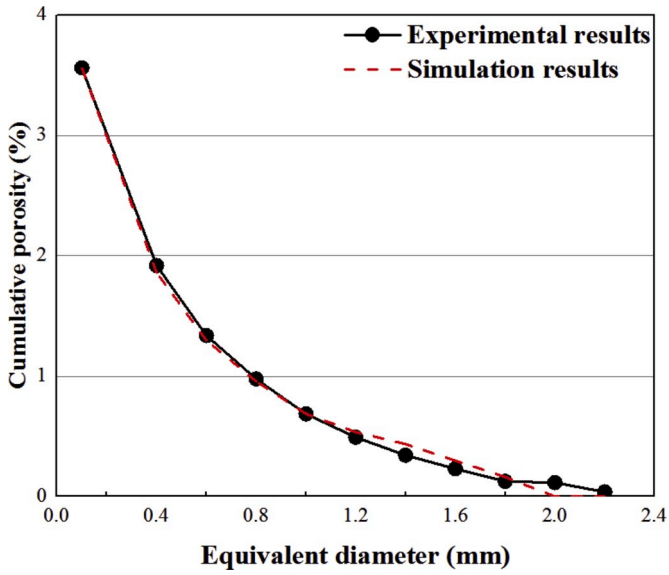

Fig. 3. Cumulative porosities of experimental and simulated material structures.

the meso-scale.

3.1. Entrapped air voids

Entrapped air voids act as initial flaws in the material structure and have a considerable influence on the mechanical properties of the specimen [58]. Therefore, it is essential to explicitly consider them in the model. The porosity and pore size distribution were determined by X-ray computed tomography (XCT) scanning and image processing techniques.

For the XCT scanning, a cylindrical specimen (24 mm diameter, 39 mm height) as described in Section 2.1 was used. During the scanning, voltage of 150 KeV and current of 150 μA for the X-ray source tube was used. Spatial resolution was set to 100 μm/voxel. After image reconstruction, a global thresholding method using the "over-flow" point as described in Ref. [64] was implemented to segment the pores from initial greyscale level based images. This results in a porosity of 3.56%, which is in accordance with Ref. [65]. Assuming spherical shape for entrapped air voids, the experimental pore size distribution was be obtained (see Fig. 3). The experimentally characterized porosity and its pore size distributions were then used as reference to generate the database of the air voids (diameter range: 0.2 mm–2.4 mm) which were to be placed into a pre-defined domain of the numerical model (10 mm × 10 mm × 10 mm).

3.2. Irregular sand particles

It is well-known that the shape and size of aggregate particles in the model have a significant influence on the simulated mechanical performance of mortar or concrete [24,44,66]. In order to have a quantitative prediction of the material behaviour, realistic aggregate shape and size should be used. It has been shown that spherical harmonic series is an effective mathematical tool to characterize the shape of particles analytically. The procedures to describe particle shape characterizations for a given class of aggregates from XCT scans have been established [67]. Statistical methods have also been developed to generate new particles based on statistics that have been obtained from a real particle dataset or elsewhere [68,69]. In this work, the Anm model [61] has been used to pack sand particles with realistic shapes into the domain of the numerical model. An example of an irregularly-shaped particle described mathematically by the spherical harmonic

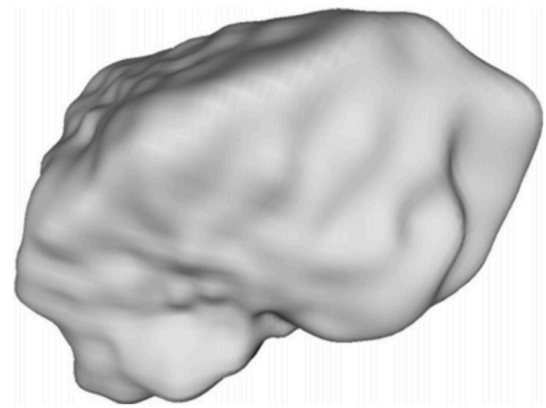

Fig. 4. An irregular shape sand particle created by Anm model [61].

expansion is shown in Fig. 4. More details about this model are available in the literature [61]. The aggregates were selected from a dataset containing 806 crushed sand particles and scaled up or down (using pseudo-random number based algorithms) to the size between 1 mm and 2 mm and placed into the pre-defined domain (10 mm × 10 mm × 10 mm) one after another until reaching the prescribed volume ratio.

In order to properly model the aggregate structure in mortar, the realistic volumetric ratio of sand should be considered. According to the mixture design, the volumetric ratio of sand is calculated as follows: Given that the specific gravity of sand and cement is 2.60 kg/m^3 and 3.15 kg/m^3 respectively, the volumetric ratio of cement: sand: water is: (1/3.15): 0.7/2.60: 0.3 = 0.317:0.269:0.3. On a percentage basis, the volumes are as follows: cement (dry) = 35.803; sand = 30.363; water = 33.834. In terms of the given case, 70% of the cement has hydrated after 28 days [62]. Consequently, continuing in percentage volume units, the volume of anhydrous cement equals 10.741 and the volume of hydrated cement 25.062. Assuming volume of combined water is 0.23 [65] of the mass of hydrated cement, i.e. 0.23 × 25.062 × 3.15 = 18.157 and the free water is 15.677. On hydration, the volume of the solid products of hydration becomes smaller than the sum of volumes of the constituent cement and water by 0.254 of the volume of combined water [65]. Hence, the volume of the solid products of hydration is: 25.062 + (1–0.254) × 18.157 = 38.607. Because the air content is 3.56% as measured by XCT, the volume of the remaining materials must add up to 0.96.44 of the total volume of mortar. Therefore, the volumetric ratio of sand is: 0.9644 × (30.363)/(10.741 + 38.607+30.363 + 15.677) = 0.307.

3.3. Digital mortar specimen

In terms of placing or packing air voids and sand particles in the predefined container, no overlap was allowed. Pseudo-random number based algorithms were implemented to position and rotate the packing objects (No rotation is needed for the air voids). In order to improve the packing efficiently, large particles were placed first. Considering the realistic specimen was sawn from the cylinder, to avoid the "wall effect" when depositing the aggregates, periodic boundary conditions were applied. This permits a particle to pass through the surface of the simulation box and the part outside the simulation box is put on the opposite surface by placing a duplicate particle with the same orientation. After packing, the simulated vector-based composite geometrical structure was digitalized into the digital specimens with a resolution of 100 μm/voxel, resulting in a 100 × 100 × 100 voxels microstructure, see Fig. 5. The resolution was chosen on purpose to match the size of the investigated material volume at micro-scale from the authors' previous works [51,54,62]. In such a way, a multi-scale fracture modelling approach developed by the authors [57,58] could be implemented.

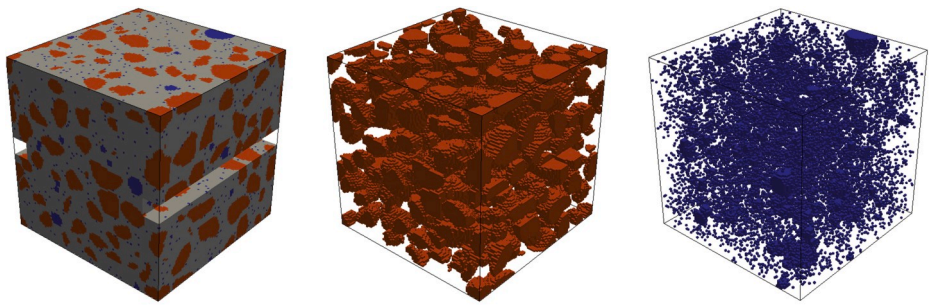

(a) (b) (c)

Fig. 5. Simulated composite geometrical structure of 10 mm mortar specimen: (a) sand particles and air voids are embed in the continuum cement paste matrix; (b) spatial distribution of sand particles; (c) spatial distribution of air voids (orange: aggregate; grey: cement paste; blue: pore). (For interpretation of the references to colour in this figure legend, the reader is referred to the Web version of this article.)

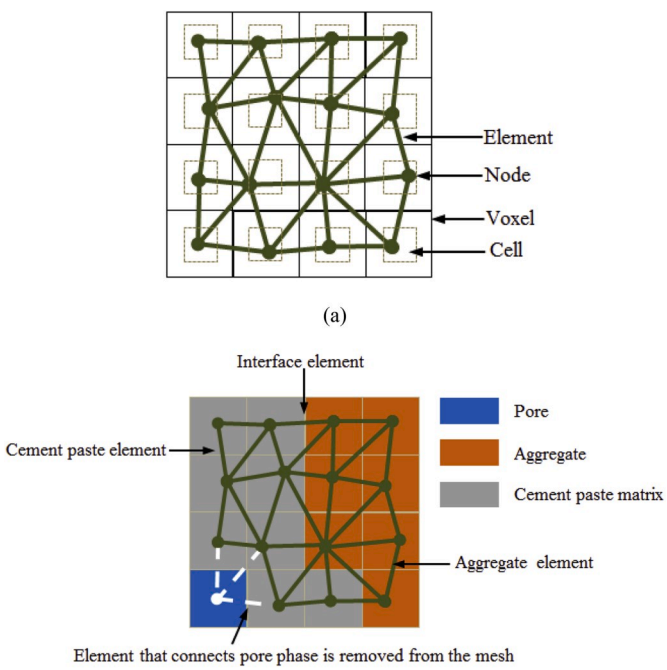

Fig. 6. Schematic view of (a) lattice network construction and (b) overlay procedure for 2D lattice mesh.

4. Deformation and fracture modelling

4.1. Basic principles of lattice model

In the lattice model, the continuum is schematized as a set of beam elements that can transfer axial forces, shear forces and bending moments. The constitutive law of each beam element can be assumed either brittle [70] or ductile [71]. For simulating the fracture process with sufficient detail, small beam element must be used. This leads to a low ratio of length and height of the used beam element, thus the Timoshenko beam element is used [3]. The mesh is loaded by a combination of external forces and displacements that act on the specimen. Then, a set of linear elastic analyses is performed by calculating the comparative stress within each element using the following equation:

$$\sigma = \frac{N}{A} + \alpha_M \frac{\max(M_X, M_Y)}{W} \tag{1}$$

where A is the beam cross-sectional area, M_x and M_y the bending moments in the local coordinate system, and W the section modulus. The parameter α_M is introduced to select a failure mode where bending plays either a dominant or a restricted role. In the past, its value has been commonly adopted as 0.05 with satisfactory results [20,72]. Consistent with the authors' previous works [57,58], this value is also adopted herein. In every analysis step, the loading is increased until exactly one beam in the mesh has a stress/strength ratio equal to one. This beam is then degenerated following the assigned constitutive law or removed from the mesh (representing a small crack) if it loses the capability for carrying load. The mesh is then updated and relaxed. This loading procedure is repeated until a pre-defined stopping criterion (e.g. load or displacement).

Digital material structure generated in Section 3 was converted to input for the lattice model by utilizing the overlay procedure as shown in Fig. 6. First, a cubic cell was defined within each voxel. A node was randomly positioned in each cell. Delaunay tessellation of the set of nodes was then applied to connect nodes with adjacent Voronoi cells by beam elements, as outlined in Ref. [73]. The cell to voxel length ratio defines the degree of randomness of the model, with a range between 0 and 1. When randomness approaches 1, the cell is identical to the voxel which means the node is randomly placed in the voxel. If a value of 0 randomness is used, the node is positioned in the centre of the voxel. The choice of mesh randomness affects the simulated fracture behaviour of material as well as the Poisson's ratio of the lattice system, as shown in Ref. [12,74]. In order to avoid large variations in the length of elements and introduce geometry disorder of texture, a randomness of 0.5 is adopted herein. This randomness results in a Poisson's ratio of 0.18 for the global system, which is close to the cementitious materials. The cross section of all beam elements is the taken to be the same. The cross section is calibrated using a system in which all elements have the same properties (elastic modulus and tensile strength). The cross section is adjusted so that the global elastic modulus of the mesh matches the local elastic modulus of the beam element.

Three types of element were defined according to the location of two ends of the element, namely: cement paste, interface and aggregate elements. This was used to define properties of each lattice element. In this way, different mechanical properties are assigned to different phases presented in the material structure. The cement paste element and the aggregate element represent the cement paste matrix and aggregate, respectively. The interface element is introduced to consider the interaction between the cement paste and the aggregate. No element is generated to connect the pore phase, which results in the initial flaws in the model.

4.2. Up-scaling the local constitutive law from micromechanical modelling

In the present study, a multi-scale modelling scheme that has been

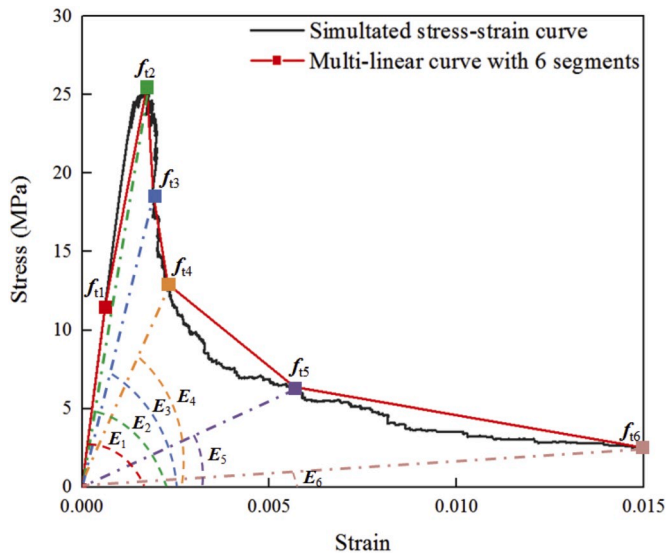

Fig. 7. Approximation of the non-linear stress-strain response of cement paste using a multi-linear curve.

developed by the authors is adopted to determine the input mechanical properties of each phase [57,58]. By properly choosing a volume size of the material structure at the smaller scale to match the resolution of the larger scale observation, the global fracture behaviour (i.e. stress-strain response under uniaxial tension) of the smaller scale simulation can be used as input for local mechanical properties at the larger scale. Note that this multi-scale scheme does not consider the representative volume element (RVE). This is because, for fracture of softening materials, an RVE might not exist due to localization issues [75].

For the sake of simplification, a perfectly elastic brittle constitutive relation is generally assumed at the element level [20,37,49,76–78]. Although it is reasonable to consider the aggregate as ideally elastic, recent advances in micromechanical modelling revealed a quasi-brittle fracture nature of cement paste at the micro-scale under both tension [51,62] and compression [63], arising from its heterogeneous microstructure. In order to investigate the influence of local softening on the global material response, both linear elastic brittle constitutive law and the one considering softening are used and compared in the current work.

4.2.1. Using step-wise softening law

In this section, a so-called step-wise approach as described in Ref. [57,71] was used to up-scale of the simulated constitutive relation of cement paste from the micro-scale. This approach approximates the original non-linear stress-strain curve with a multi-linear curve so that the element can degenerate gradually. With respect to cement paste elements, their constitutive relations were taken from the authors' previous work [62] in which uniaxial tension test was conducted on the simulated 100 μm HCP micro-cubes. As shown in Fig. 7, a multi-linear curve with six segments was used to simplify the constitutive relation and capture its characteristics. The points were taken at: (1) origin; (2) first cracking; (3) peak load; (4) first point in response for which load is <75% of the peak; (5) first point in response for which the load is <50% of the peak; (6) first point in response for which the load is <25% of the peak; (7) point for which the strain reaches 0.015. After the last point, the cement paste was regarded as failed. As reported in Ref. [62], there is significant scatter in terms of simulated micromechanical properties on the microscale in terms of the stress-strain response. To take this influence into account, 10 stress-strain curves of 0.1 mm sized specimens that have been simulated in Ref. [62] were schematized and listed Table 1. They were randomly assigned to the cement paste elements. Because the focus of this paper is to utilize the outcomes from micromechanical modelling as input for the meso-scale fracture modelling, the readers are referred to Ref. [51,52,62] for more details about the micromechanical modelling.

For the sand aggregate, a linear elastic/perfectly brittle constitutive law was used. Its elastic modulus was taken from Ref. [79], i.e. 70 GPa. Its tensile strength was assumed as 1/1000 of the modulus. This ratio is larger than observed at the meso-scale, as it is found that it increases with the length scale decreasing [58,62,80]. Moreover, in the current study, no cracking was expected in the aggregate. Consequently, strength of the aggregate has no contribution to the mechanical response of the simulated mortar.

In terms of the ITZ, an experimentally-informed approach has been proposed in the authors' previous work [54] to model the debonding process of this area (50 μm × 100 μm × 100 μm) from a quartz type aggregate under uniaxial tension. Two extreme stress-strain responses (upper and lower bound, termed as U an L respectively) were determined by an inverse analysis for one specimen using experimental data. The simulated properties from the upper bound are higher than lower bound. Two sets of input constitutive relation of ITZ were considered and implemented, respectively. As expected, these mechanical parameters (e.g. elastic modulus and tensile strength) are much lower than bulk cement paste at the same length scale due to the highly porous

Table 1
Step-wise softening relation of bulk cement paste up-scaled from the micro-scale modelling (100 μm × 100 μm × 100 μm).

Number	Mechanical parameters	Segment 1	Segment 2	Segment 3	Segment 4	Segment 5	Segment 6
1	E (GPa)	27.10	22.49	14.78	8.12	2.06	0.34
	f_t (MPa)	7.07	21.21	15.90	10.59	5.30	2.86
2	E (GPa)	29.40	24.67	16.83	10.02	2.79	0.34
	f_t (MPa)	8.23	24.67	18.50	12.34	6.14	2.38
3	E (GPa)	31.48	25.11	16.15	8.50	2.17	0.38
	f_t (MPa)	10.78	25.34	19.00	12.67	6.34	3.05
4	E (GPa)	31.86	26.63	14.60	9.52	3.26	0.22
	f_t (MPa)	6.76	22.68	17.04	11.54	5.65	1.73
5	E (GPa)	37.11	28.15	21.35	11.77	2.99	0.28
	f_t (MPa)	12.77	27.07	20.32	13.54	6.67	2.18
6	E (GPa)	35.67	28.22	18.80	10.82	2.16	0.39
	f_t (MPa)	11.49	25.55	18.66	12.94	6.39	2.81
7	E (GPa)	36.05	28.33	21.30	12.67	3.68	0.39
	f_t (MPa)	11.36	24.38	18.68	12.21	6.09	2.51
8	E (GPa)	29.92	28.37	18.86	12.48	3.98	0.38
	f_t (MPa)	11.04	25.67	19.26	12.96	6.42	2.63
9	E (GPa)	35.31	31.63	24.61	16.61	6.24	0.38
	f_t (MPa)	10.89	29.30	22.17	15.37	7.32	2.26
10	E (GPa)	33.66	32.34	27.92	14.02	4.91	0.41
	f_t (MPa)	13.36	28.07	21.44	14.27	7.03	2.56

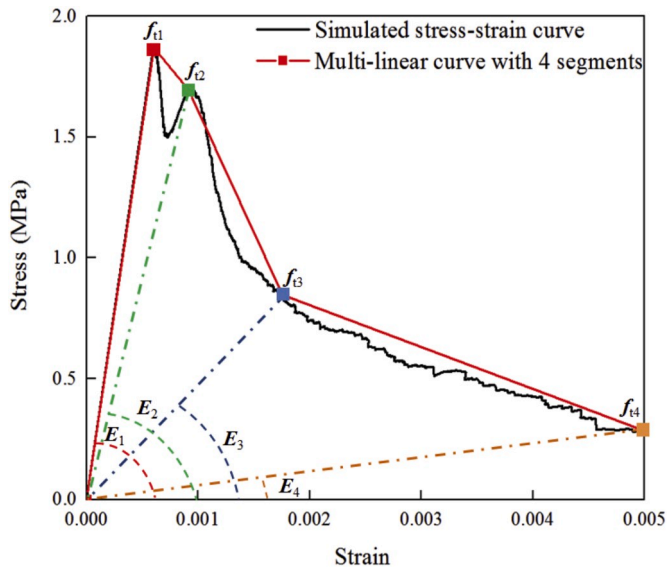

Fig. 8. Approximation of the non-linear stress-strain response of ITZ using a multi-linear curve.

Table 2
Step-wise softening relation of ITZ (case L) up-scaled from the lower boundary micro-scale modelling in Ref. [54] (50 μm × 100 μm × 100 μm).

Element type	Mechanical parameters	Segment 1	Segment 2	Segment 3	Segment 4
1	E (GPa)	5.91	3.61	0.96	0.11
	f_t (MPa)	1.87	1.69	0.85	0.29
2	E (GPa)	7.31	4.13	1.33	0.10
	f_t (MPa)	2.29	1.94	0.97	0.25
3	E (GPa)	8.58	4.74	1.48	0.01
	f_t (MPa)	2.68	2.25	1.12	0.03
4	E (GPa)	5.28	3.22	0.81	0.12
	f_t (MPa)	1.65	1.54	0.77	0.29
5	E (GPa)	6.62	3.88	1.21	0.02
	f_t (MPa)	2.08	1.82	0.91	0.06
6	E (GPa)	7.13	4.31	1.32	0.04
	f_t (MPa)	2.32	2.05	1.03	0.10
7	E (GPa)	5.87	3.48	1.03	0.03
	f_t (MPa)	1.82	1.64	0.82	0.08
8	E (GPa)	6.28	3.65	0.94	0.01
	f_t (MPa)	1.95	1.68	0.84	0.03
9	E (GPa)	6.52	3.94	1.10	0.12
	f_t (MPa)	2.08	1.87	0.93	0.29
10	E (GPa)	7.62	4.50	1.27	0.07
	f_t (MPa)	2.44	2.08	1.04	0.18

microstructure. The stress-strain curve was schematized as a multi-linear curve with four segments as shown in Fig. 8. Unlike the cement paste, the ITZ specimens have two peaks in the simulated stress-strain response. Therefore, their stress-strain relationship was simplified as multi-linear using five points taken at: (1) origin; (2) peak load; (3) second peak load; (4) first point in response for which the load is <50% of the peak; (5) point for which the strain reaches 0.005. To consider the heterogeneity, for each set, 10 specimens that have been simulated in Ref. [54] were schematized and used as input in the current study. As shown in Fig. 6, the interface element comprises a piece of aggregate and a piece of cement paste as well as the ITZ. The strength of this element was assumed as the bonding strength between the ITZ and aggregate derived from Ref. [54], while its modulus $E_{\text{interface}}$ is considered using a Reuss (series) model [3]:

$$\frac{2}{E_{\text{interface}}} = \frac{1}{E_{ITZ}} + \frac{1}{E_{\text{aggregate}}} \tag{2}$$

Table 3
Step-wise softening relation of the ITZ (case U) up-scaled from the upper boundary micro-scale modelling in Ref. [54] (50 μm × 100 μm × 100 μm).

Element type	Mechanical parameters	Segment 1	Segment 2	Segment 3	Segment 4
1	E (GPa)	8.22	5.06	1.36	0.16
	f_t (MPa)	3.12	2.82	1.42	0.48
2	E (GPa)	10.13	5.78	1.88	0.14
	f_t (MPa)	3.82	3.23	1.62	0.42
3	E (GPa)	11.85	6.62	2.09	0.01
	f_t (MPa)	4.47	3.75	1.87	0.05
4	E (GPa)	7.36	4.52	1.14	0.17
	f_t (MPa)	2.75	2.57	1.28	0.48
5	E (GPa)	9.19	5.43	1.71	0.03
	f_t (MPa)	3.47	3.03	1.52	0.10
6	E (GPa)	9.89	6.03	1.86	0.06
	f_t (MPa)	3.87	3.42	1.72	0.17
7	E (GPa)	8.17	4.88	1.45	0.04
	f_t (MPa)	3.03	2.73	1.37	0.13
8	E (GPa)	8.73	5.11	1.33	0.01
	f_t (MPa)	3.25	2.80	1.40	0.05
9	E (GPa)	9.06	5.51	1.55	0.17
	f_t (MPa)	3.47	3.12	1.55	0.48
10	E (GPa)	10.55	6.29	1.79	0.10
	f_t (MPa)	4.07	3.47	1.73	0.30

Table 4
Linear-elastic constitutive relation of cement paste up-scaled from the micro-scale modelling (100 μm × 100 μm × 100 μm) [62].

Element type	Young's modulus E (GPa)	Tensile strength ft (MPa)
1	27.10	21.21
2	29.40	24.67
3	31.48	25.34
4	31.86	22.68
5	37.11	27.07
6	35.67	25.55
7	36.05	24.38
8	29.92	25.67
9	35.31	29.30
10	33.66	28.07

where E_{ITZ} and $E_{\text{aggregate}}$ are elastic moduli corresponding to the ITZ and the aggregate, respectively. The resulting two sets of constitutive relations of the interface elements are listed in Table 2 and Table 3 respectively. Values in Tables 2 and 3 were then assigned to the interface elements randomly in simulations termed as case L and case U, respectively.

4.2.2. Using linear-elastic brittle constitutive relation

A simulation (termed as case E) using linear-elastic brittle constitutive relation for local elements is performed as a comparison with the case U and the case L. When a linear-elastic brittle constitutive relation is used, the element will be removed from the mesh immediately once the stress reaches its strength. The required input parameters are Young's

Table 5
Linear-elastic constitutive relation of ITZ up-scaled from the upper boundary micro-scale modelling in Ref. [54] (50 μm × 100 μm × 100 μm).

Element type	Young's modulus E (GPa)	Tensile strength ft(MPa)
1	8.22	3.12
2	10.13	3.82
3	11.85	4.47
4	7.36	2.75
5	9.19	3.47
6	9.89	3.87
7	8.17	3.03
8	8.73	3.25
9	9.06	3.47
10	10.55	4.07

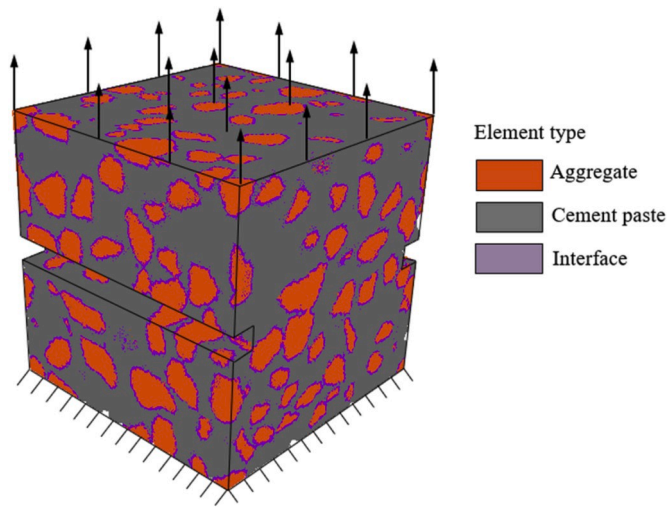

Fig. 9. Boundary condition of the computational uniaxial tension test of the mortar.

modulus and tensile strength (no compressive failure is allowed for the local elements in the current study). Input parameters for cement paste elements are listed in Table 4. As they were calculated from the same stress-strain curves that are used to consider softening, the elastic moduli and strengths are same as segment 1 and segment 2 in Table 1, respectively. The properties of aggregate elements remain unchanged (elastic modulus: 70 GPa; tensile strength: 70 MPa). For ITZ, only the simulated stress-strain curves from upper boundaries were used. The input parameters (see Table 5) for interface elements were determined using Equation (2), which is equal to values in segment 1 in Table 3.

4.3. Boundary conditions

As shown in Fig. 9, the computational uniaxial tension test was performed by applying nodal displacement at one end and fixing the other. Because fixed plates are used in the experiment, the rotations at the ends are restricted in the simulation. To consider the restrictions introduced by the high stiffness of steel plates, no lateral deformation is allowed at both ends in the model.

5. Results and discussion

5.1. Experimental results

Three specimens were prepared and tested. One fractured specimen is shown in Fig. 10. It is clear that the specimen cracked in the middle where two notches exist. Due to the heterogeneity of the material structure, the crack surface is quite tortuous. The measured load-displacement curves are shown in Fig. 11. As the test is performed under displacement control using LVDT's, the fracture process was stable after the peak and typical quasi-brittle behaviour is observed. Before the peak, the load increases monotonically with displacement, and decreases in the post-peak branch. A four-stage fracture model [1] can be used to describe the measured load-displacement curves. Before the peak, the material is linear elastic in stage I (below 0.2 kN, in this case), after which the stiffness decreases gradually (stage II). After the peak, a significant load drop (stage III) is observed, followed by a long shallow tail. The measured load-displacement curves and the observed failure pattern are further used to validate the adopted modelling strategy. More details about the fracture propagation can be obtained by the simulation and used to explain the observed load-displacement response.

Table 6 shows the Young's modulus, strength and fracture energy calculated from the load-displacement curves. The modulus is calculated from the linear-elastic stage. Strength is derived from the peak load. Fracture energy is derived from the post-peak branch using equation:

$$G_f = \int_{u1}^{u2} \sigma du \tag{3}$$

where σ is the stress, u the displacement, u_1 displacement at peak stress, u_2 the displacement at failure. The maximum displacement u_2 used for the calculation is 20 μm. As the specimen is 4 times larger than the biggest aggregate (2 mm), small variations occur in the measured Young's moduli and strengths [2]. A large deviation (coefficient of variation > 0.1) is observed in terms of the fracture energy, because the post-peak response is governed by the crack localization process, which can be disturbed by the flaws or stiff aggregate present in the matrix.

5.2. Modelling results

The simulated load-displacement responses are compared with the experimental measurements in Fig. 12. The calculated elastic modulus, tensile strength and fracture energy (using Equation (3)) are listed in Table 7. In terms of case E, it can reproduce the load-displacement response in a qualitative sense using linear-elastic brittle constitutive

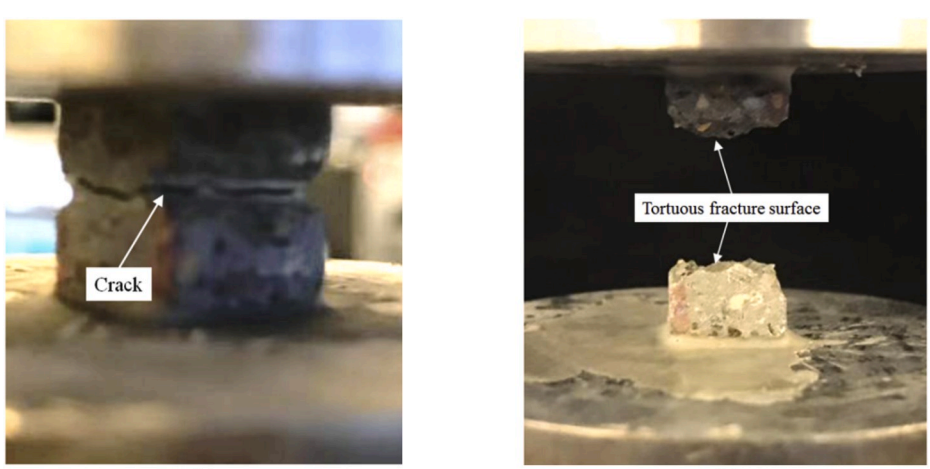

(a) (b)

Fig. 10. Fractured specimens under uniaxial tension: (a) side of view; (b) front view.

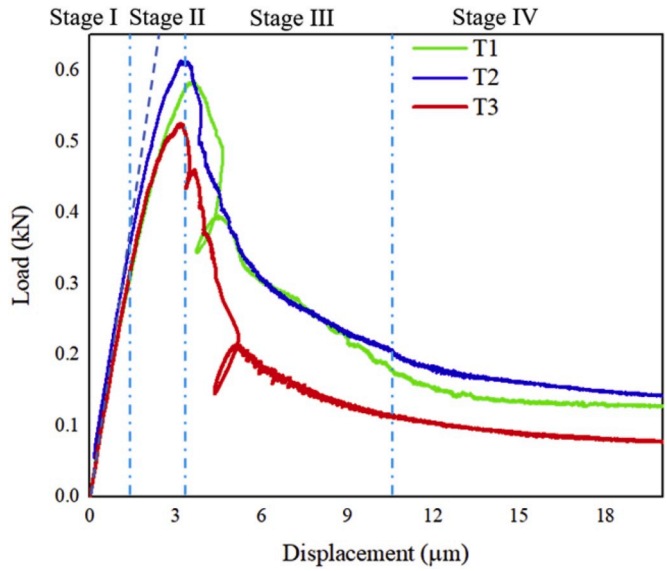

Fig. 11. Experimentally measured load-displacement curves of the 10 mm specimens.

Table 6
Measured mechanical properties of the 10 mm mortar specimens.

Sample	Young's modulus (GPa)	Tensile strength (MPa)	Fracture energy (J/m^2)
T1	26.38	5.84	29.28
T2	26.85	6.14	33.38
T3	25.84	5.25	19.80
Average	26.36	5.74	27.49
Coefficient of variation	0.015	0.064	0.2069

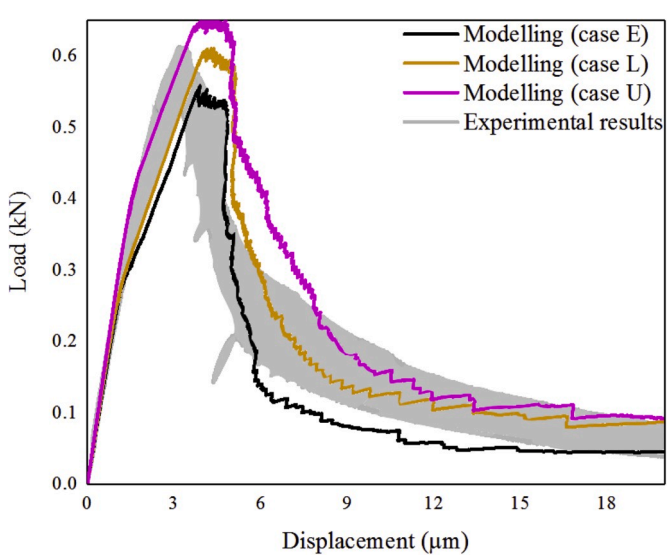

Fig. 12. Comparison between the measured and simulated load-displacement curves.

relation. The predicted Young's modulus (27.67 MPa) and the tensile strength (5.56 MPa) are in accordance with experimental measurements. However, the fracture energy (17.36 J/m^2) is much lower. In sense of quantitative analysis, the simulated stiffness of case E decreases more than the experimental results in stage II. As shown in Fig. 12a, a significant reduction of the slope can be observed at the end of stage I,

Table 7
Simulated mechanical properties of the 10 mm mortar specimens.

Simulation	Young's modulus (GPa)	Tensile strength (MPa)	Fracture energy (J/m^2)
Case E	27.67	5.56	17.36
Case L	25.96	6.07	25.29
Case U	27.67	6.50	31.84

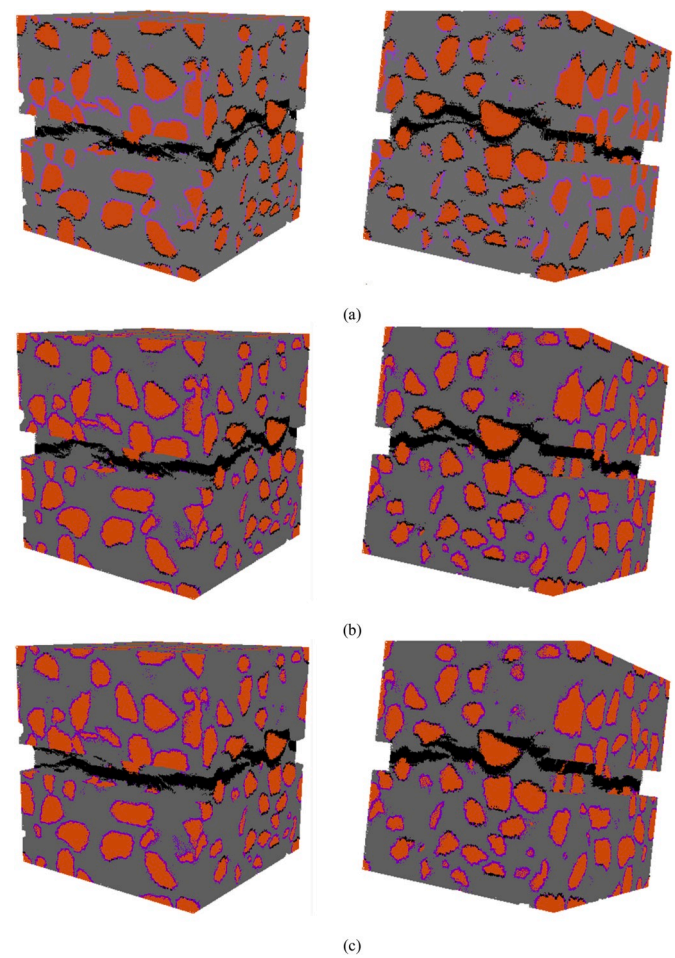

Fig. 13. Comparison between the simulated fractured specimens at failure stage: (a) case E; (b) case L; case U (left: view from the notch side; right: view from the non-notched side. black: crack).

which indicates that a lot of interface elements crack under the same load, which is not realistic. Furthermore, a steeper drop in stage III and a long tail with lower load are observed. This leads to the lower fracture energy compared with experimental results. In previous studies, this brittleness of the lattice modelling results was attributed to the following: (1) the inability of the 2D model to simulate 3D effects, in the early days of the lattice model; (2) the use of a relatively coarse mesh unable to explicitly consider the influence of small aggregates [74,81]. First, more crack branches and overlaps can occur in a 3D compared to 2D. This enables a more stable crack development and more ductile post-peak behaviour. In the current study, these influences have been eliminated by using *only* sand particles larger than 1 mm in both the modelled material structure and the real material, and a 3D mesh with relatively high resolution (0.1 mm). The brittleness present in case E can therefore not be attributed to any of the two aforementioned influences: instead, it can only result from the adopted linear-elastic constitutive relation, which neglects the local softening of the cement paste and the interface.

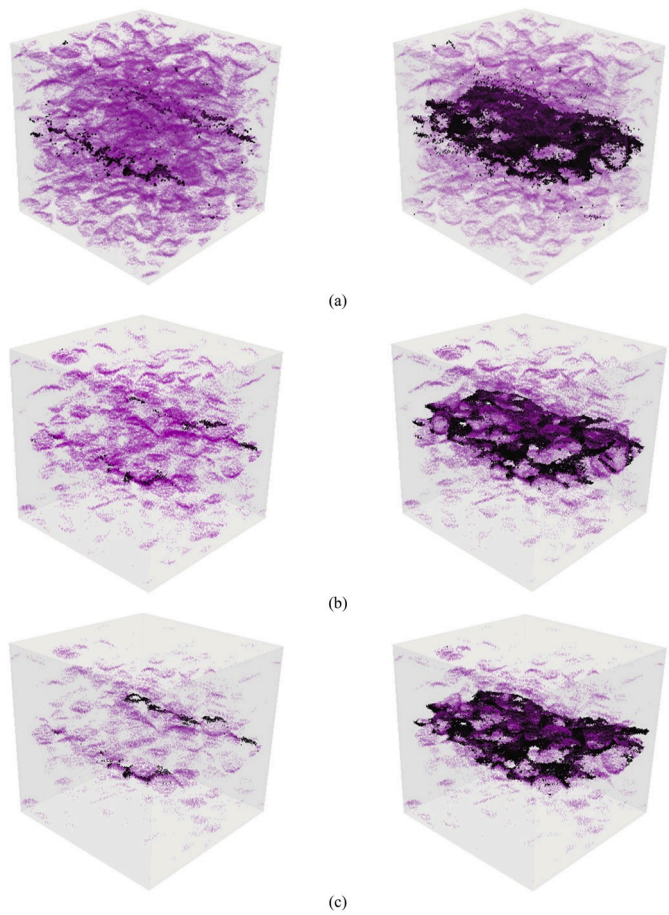

Fig. 14. Comparison between the simulated crack patterns at peak and failure stage: (a) case E; (b) case L; case U (left: crack pattern at peak; right: crack pattern at failure stage; violet: cracked interface element; black: cracked cement paste element). (For interpretation of the references to colour in this figure legend, the reader is referred to the Web version of this article.)

Consequently, the simulated load-displacement curves (case L and case U) using the step-wise approach are closer to the experimental results. The simulated Young's modulus, strength and fracture energy for case U and case L in Table 7 show a reasonable agreement with the experimental results in Table 6. Therefore, in sense of quantitative prediction of fracture process of mortar at the meso-scale, the step-wise softening law has to be used for cement paste matrix and ITZ phase to consider the influence of heterogeneity at the micro-scale. As higher strengths and Young's moduli are assigned to interface elements in case U, the simulated mechanical properties of case U are higher than case L. Furthermore, it is worth mentioning that, in case L, the first segment of interface element has lower moduli and strengths compared with case E. Nevertheless, case L has a higher stiffness and peak load in stage II than case E as well as a more ductile post-peak response.

To explain the observed load-displacement responses, the simulated fractured specimens at failure stage and fracture patterns at peak and failure stage are compared in Fig. 13 and Fig. 14 respectively. Table 8 summarizes the number of completely cracked elements (i.e. those removed from the mesh) shown in Fig. 14. In general, all three simulations show similar main cracks, in accordance with the experimental observations. However, case U has the fewest cracked interface elements compared with the others, resulting in the lowest stiffness reduction in stage II and more ductile behaviour after the peak. As shown in Fig. 14a and Table 8, at the peak load stage, almost 40% of interface elements are cracked in Case E, leads to the brittle load-displacement response after the peak. However, these isolated microcracks (cracks at the interface) cannot be observed by common experimental techniques. For example, Scanning Electron Microscopy requires impregnation and polishing of the specimens. During impregnation, the epoxy is not able to penetrate isolated cracks. Therefore, these microcracks cannot be observed using such technique. A possibility would be to use In-situ XCT scanning. However, the resolution of scanning is not high enough and there remains a challenge on the segmentation between aggregate and cement paste.

Compared to experiments, an advantage of the numerical model is that it is able to show the detailed fracture pattern at all loading stages. The simulated fracture patterns of case U at different loading stages are therefore used to further explain the obtained load-displacement response, see Fig. 15. Fig. 16a shows the crack pattern corresponding to point a in Fig. 15. Clearly, up to the end of the linear-elastic stage, only interface elements crack completely. No cracking occurs in the cement paste matrix. With the load increasing, micro-cracks start to nucleate and grow in the bulk cement paste around the notches (see Fig. 16b). This leads to the curved pre-peak load-displacement diagram. At the peak load, two macro-cracks are observed at the notches (Fig. 16c). Two cracks are then formed as macro-cracks (see Fig. 16d and e) in stage III, leading to a significant drop of the load bearing capacity of the material. As shown in Fig. 16f, the overlap between the two main cracks leads to the long tail before failure.

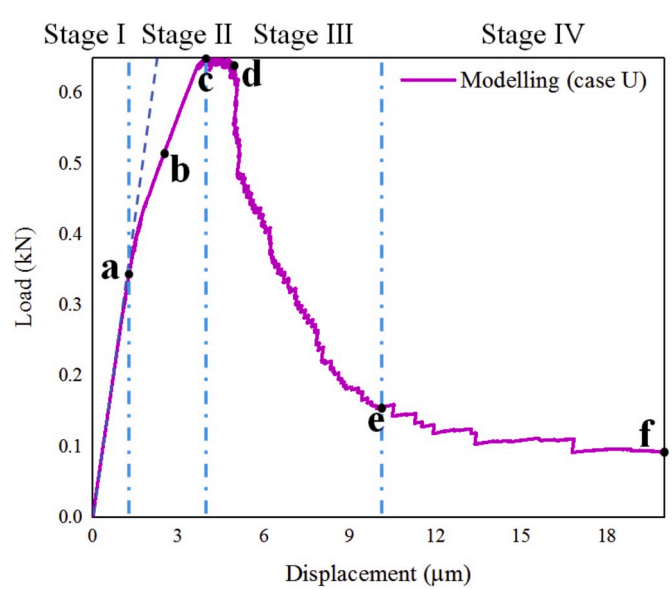

Fig. 15. Critical loading stages from which the fracture pattern are shown in Fig. 16.

Table 8
Summary of totally cracked elements at different fracture stages.

Simulation	Cracked elements at peak			Cracked elements at failure stage		
	Interface	Cement paste	Aggregate	Interface	Cement paste	Aggregate
Case E	268657	1839	0	316769	49584	0
Case L	44664	877	0	90437	30086	0
Case U	23764	1304	0	64617	38126	0

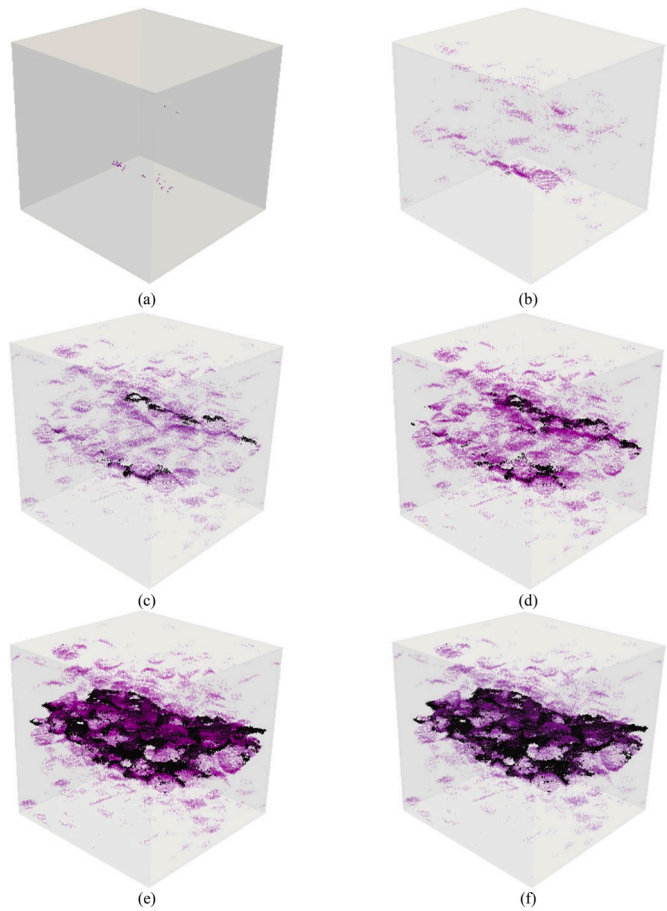

Fig. 16. Simulated fracture pattern of case E at different loading stage in Fig. 10.10: (a) point a, end of the linear-elastic stage; (b) point b, middle point at stage II; (c) point c, peak load; (d) point d, at which load starts decreasing significantly; (e) point e, start of the long shallow tail; (f) point f, material failures. (only cracked elements are plotted: violet - interface element; dark - cement paste element). (For interpretation of the references to colour in this figure legend, the reader is referred to the Web version of this article.)

Additionally, it is worth mentioning that the proposed multi-scale modelling approach has been successfully validated by experimental measurements. By upscaling the modelling results from the micro-scale, this approach can reproduce the experimental results well without further calibration. This means that the model at the meso-scale can become quantitatively predictive by following the multi-scale strategies proposed in this work. However, due to the high computational requirement, the influence of smaller sand particles is not studied in this work. This could be overcome by more powerful computational facilities and/or more efficient numerical algorithms in the future. Note that the scope of the current paper is limited to monotonic loading. The sequentially-linear procedure used herein does not allow for non-proportional loading and cases such as unloading. However, with recent development of improved sequentially linear methods for non-proportional loading [82,83] and the fatigue and creep test carried out at the micro-scale [53,84], it is believed that the behaviour of meso-scale specimens under cyclic loading can be modelled in a similar way in the future.

6. Conclusions

In this work, numerical simulations and experimental measurements were compared to validate the proposed multi-scale modelling scheme for mortar at the meso-scale. Special attention was paid to make the material structure of real and virtual mortar composites comparable. The input constitutive relations for the cement paste (matrix and ITZ) were derived from the recent micromechanical modelling results. Two types of constitutive relations (linear-elastic and step-wise softening) were assumed. It was shown that the model which considers the strain-softening of cement paste can reproduce the experimental measured load-displacement response well in a quantitative sense. Besides, other conclusions can be drawn:

- When using a linear-elastic/brittle constitutive relation of cement paste, the fracture process of mortar composites can be modelled in a qualitative sense. This model is able to predict the Young's modulus and tensile strength of mortar. However, many cracks occur in the cement-aggregate interface before crack localization starts, leading to unrealistic brittle response in the non-elastic stage and lower fracture energy compared with the experiments.
- The heterogeneous nature of cement paste at the micro-scale is important for the non-elastic behaviour of mortar composites at the meso-scale. This heterogeneity results in strain-softening behaviour at the micro-scale, which must be considered in the meso-scale model for quantitative prediction of fracture behaviour of cementitious composites (mortar or concrete).

The experimentally validated micromechanical models from the previous work of the authors [51,54,57,62] are able to provide required information for the meso-scale model. This reduces the burden on calibration for the meso-scale model, and offers the opportunity for the meso-scale model to become fully predictive. Moreover, the proposed multi-scale modelling approach is generic, and can be extended to predict composites with different type of aggregates and binder materials.

Declaration of competing interest

The authors declare no conflict of interest.

Acknowledgement

Hongzhi Zhang, Yading Xu, Yidong Gan would like to acknowledge the funding supported by China Scholarship Council under grant number 201506120067, 201708110187 and 201706130140 respectively. Hongzhi zhang would like to acknowledge the Taishan Scholars Program of Shandong Province (tsqn201909032).

References

[1] J.G. Van Mier, Concrete Fracture: a Multiscale Approach, CRC press, 2012.
[2] O. Bernard, F.-J. Ulm, E. Lemarchand, A multiscale micromechanics-hydration model for the early-age elastic properties of cement-based materials, Cement Concr. Res. 33 (9) (2003) 1293–1309.
[3] Z. Qian, Multiscale Modeling of Fracture Processes in Cementitious Materials, Delft University of Technology, Delft, The Netherlands, 2012.
[4] Z. Qian, E. Schlangen, G. Ye, K. van Breugel, Modeling framework for fracture in multiscale cement-based material structures, Materials 10 (6) (2017) 587.
[5] F. Bernard, S. Kamali-Bernard, W. Prince, 3D multi-scale modelling of mechanical behaviour of sound and leached mortar, Cement Concr. Res. 38 (4) (2008) 449–458.
[6] V.P. Nguyen, M. Stroeven, L.J. Sluys, Multiscale failure modeling of concrete: micromechanical modeling, discontinuous homogenization and parallel computations, Comput. Methods Appl. Mech. Eng. 201–204 (2012) 139–156.
[7] E.A. Rodrigues, O.L. Manzoli, L.A. Bitencourt Jr., T.N. Bittencourt, M. Sánchez, An adaptive concurrent multiscale model for concrete based on coupling finite elements, Comput. Methods Appl. Mech. Eng. 328 (2018) 26–46.
[8] B. Sun, Z. Li, Adaptive concurrent multi-scale FEM for trans-scale damage evolution in heterogeneous concrete, Comput. Mater. Sci. 99 (2015) 262–273.
[9] P. Chaudhuri, Multi-scale modeling of fracture in concrete composites, Compos. B Eng. 47 (2013) 162–172.
[10] V.P. Nguyen, M. Stroeven, L.J. Sluys, An enhanced continuous–discontinuous multiscale method for modeling mode-I cohesive failure in random heterogeneous quasi-brittle materials, Eng. Fract. Mech. 79 (2012) 78–102.
[11] J.S. Dolado, K. Van Breugel, Recent advances in modeling for cementitious materials, Cement Concr. Res. 41 (7) (2011) 711–726.
[12] E. Schlangen, E. Garboczi, Fracture simulations of concrete using lattice models: computational aspects, Eng. Fract. Mech. 57 (2) (1997) 319–332.

[13] J.E. Bolander, S. Saito, Fracture analyses using spring networks with random geometry, Eng. Fract. Mech. 61 (5) (1998) 569–591.
[14] E.P. Prado, J.G.M. van Mier, Effect of particle structure on mode I fracture process in concrete, Eng. Fract. Mech. 70 (14) (2003) 1793–1807.
[15] G. Cusatis, Z.P. Bažant, L. Cedolin, Confinement-shear lattice model for concrete damage in tension and compression: I. Theory, J. Eng. Mech. 129 (12) (2003) 1439–1448.
[16] P. Grassl, M. Jirásek, Meso-scale approach to modelling the fracture process zone of concrete subjected to uniaxial tension, Int. J. Solid Struct. 47 (7–8) (2010) 957–968.
[17] E. Schlangen, J.G.M. van Mier, Experimental and numerical analysis of micromechanisms of fracture of cement-based composites, Cement Concr. Compos. 14 (2) (1992) 105–118.
[18] G. Cusatis, D. Pelessone, A. Mencarelli, Lattice discrete particle model (LDPM) for failure behavior of concrete. I: theory, Cement Concr. Compos. 33 (9) (2011) 881–890.
[19] D. Asahina, E.N. Landis, J.E. Bolander, Modeling of phase interfaces during pre-critical crack growth in concrete, Cement Concr. Compos. 33 (9) (2011) 966–977.
[20] G. Lilliu, J.G. van Mier, 3D lattice type fracture model for concrete, Eng. Fract. Mech. 70 (7–8) (2003) 927–941.
[21] W. Ren, Z. Yang, R. Sharma, C. Zhang, P.J. Withers, Two-dimensional X-ray CT image based meso-scale fracture modelling of concrete, Eng. Fract. Mech. 133 (2015) 24–39.
[22] X. Wang, Z. Yang, A.P. Jivkov, Monte Carlo simulations of mesoscale fracture of concrete with random aggregates and pores: a size effect study, Construct. Build. Mater. 80 (2015) 262–272.
[23] X. Wang, M. Zhang, A.P. Jivkov, Computational technology for analysis of 3D meso-structure effects on damage and failure of concrete, Int. J. Solid Struct. 80 (2016) 310–333.
[24] W. Trawiński, J. Tejchman, J. Bobiński, A three-dimensional meso-scale modelling of concrete fracture, based on cohesive elements and X-ray μCT images, Eng. Fract. Mech. 189 (2018) 27–50.
[25] O. Yılmaz, J.-F. Molinari, A mesoscale fracture model for concrete, Cement Concr. Res. 97 (2017) 84–94.
[26] I. Carol, C.M. López, O. Roa, Micromechanical analysis of quasi-brittle materials using fracture-based interface elements, Int. J. Numer. Methods Eng. 52 (1-2) (2001) 193–215.
[27] P. Wriggers, S.O. Moftah, Mesoscale models for concrete: homogenisation and damage behaviour, Finite Elem. Anal. Des. 42 (7) (2006) 623–636.
[28] M.G.A. Tijssens, L.J. Sluys, E. van der Giessen, Simulation of fracture of cementitious composites with explicit modeling of microstructural features, Eng. Fract. Mech. 68 (11) (2001) 1245–1263.
[29] L. Snozzi, A. Caballero, J.F. Molinari, Influence of the meso-structure in dynamic fracture simulation of concrete under tensile loading, Cement Concr. Res. 41 (11) (2011) 1130–1142.
[30] L. Struble, J. Skalny, S. Mindess, A review of the cement-aggregate bond, Cement Concr. Res. 10 (2) (1980) 277–286.
[31] B. Barnes, S. Diamond, W. Dolch, The contact zone between Portland cement paste and glass "aggregate" surfaces, Cement Concr. Res. 8 (2) (1978) 233–243.
[32] K.L. Scrivener, A.K. Crumbie, P. Laugesen, The interfacial transition zone (ITZ) between cement paste and aggregate in concrete, Interface Sci. 12 (4) (2004) 411–421.
[33] S. Diamond, J. Huang, The ITZ in concrete–a different view based on image analysis and SEM observations, Cement Concr. Compos. 23 (2–3) (2001) 179–188.
[34] A. Delagrave, J. Bigas, J. Ollivier, J. Marchand, M. Pigeon, Influence of the interfacial zone on the chloride diffusivity of mortars, Adv. Cement Base Mater. 5 (3–4) (1997) 86–92.
[35] G. Lilliu, J.G.M. van Mier, On the relative use of micro-mechanical lattice analysis of 3-phase particle composites, Eng. Fract. Mech. 74 (7) (2007) 1174–1189.
[36] J. Kozicki, J. Tejchman, Modelling of fracture process in concrete using a novel lattice model, Granul. Matter 10 (5) (2008) 377–388.
[37] H.-K. Man, J. Van Mier, Damage distribution and size effect in numerical concrete from lattice analyses, Cement Concr. Compos. 33 (9) (2011) 867–880.
[38] G. Cusatis, A. Mencarelli, D. Pelessone, J. Baylot, Lattice discrete particle model (LDPM) for failure behavior of concrete. II: calibration and validation, Cement Concr. Compos. 33 (9) (2011) 891–905.
[39] G. Ruiz, A. Pandolfi, M. Ortiz, Three-dimensional cohesive modeling of dynamic mixed-mode fracture, Int. J. Numer. Methods Eng. 52 (1-2) (2001) 97–120.
[40] A. Caballero, C.M. López, I. Carol, 3D meso-structural analysis of concrete specimens under uniaxial tension, Comput. Methods Appl. Mech. Eng. 195 (52) (2006) 7182–7195.
[41] A. Caballero, I. Carol, C.M. López, A meso-level approach to the 3D numerical analysis of cracking and fracture of concrete materials, Fatig. Fract. Eng. Mater. Struct. 29 (12) (2006) 979–991.
[42] J.M. Sancho, J. Planas, A.M. Fathy, J.C. Gálvez, D.A. Cendón, Three-dimensional simulation of concrete fracture using embedded crack elements without enforcing crack path continuity, Int. J. Numer. Anal. Model. 31 (2) (2007) 173–187.
[43] X. Su, Z. Yang, G. Liu, Finite element modelling of complex 3D static and dynamic crack propagation by embedding cohesive elements in abaqus, Acta Mech. Solida Sin. 23 (3) (2010) 271–282.
[44] S.-M. Kim, R.K. Abu Al-Rub, Meso-scale computational modeling of the plastic-damage response of cementitious composites, Cement Concr. Res. 41 (3) (2011) 339–358.
[45] S. Shahbeyk, M. Hosseini, M. Yaghoobi, Mesoscale finite element prediction of concrete failure, Comput. Mater. Sci. 50 (7) (2011) 1973–1990.
[46] Y. Huang, Z. Yang, W. Ren, G. Liu, C. Zhang, 3D meso-scale fracture modelling and validation of concrete based on in-situ X-ray Computed Tomography images using damage plasticity model, Int. J. Solid Struct. 67–68 (2015) 340–352.
[47] M. Zhang, A.P. Jivkov, Microstructure-informed modelling of damage evolution in cement paste, Construct. Build. Mater. 66 (2014) 731–742.
[48] M. Zhang, A.P. Jivkov, Micromechanical modelling of deformation and fracture of hydrating cement paste using X-ray computed tomography characterisation, Compos. B Eng. 88 (2016) 64–72.
[49] M. Luković, E. Schlangen, G. Ye, Combined experimental and numerical study of fracture behaviour of cement paste at the microlevel, Cement Concr. Res. 73 (2015) 123–135.
[50] T.-S. Han, X. Zhang, J.-S. Kim, S.-Y. Chung, J.-H. Lim, C. Linder, Area of lineal-path function for describing the pore microstructures of cement paste and their relations to the mechanical properties simulated from μ-CT microstructures, Cement Concr. Compos. 89 (2018) 1–17.
[51] H. Zhang, B. Šavija, S. Chaves Figueiredo, M. Lukovic, E. Schlangen, Microscale testing and modelling of cement paste as basis for multi-scale modelling, Materials 9 (11) (2016) 907.
[52] H. Zhang, B. Šavija, E. Schlangen, Combined experimental and numerical study on micro-cube indentation splitting test of cement paste, Eng. Fract. Mech. 199 (2018) 773–786.
[53] Y. Gan, H. Zhang, B. Šavija, E. Schlangen, K. van Breugel, Static and fatigue tests on cementitious cantilever beams using nanoindenter, Micromachines 9 (12) (2018) 630.
[54] H. Zhang, Y. Gan, Y. Xu, S. Zhang, E. Schlangen, B. Šavija, Experimentally informed fracture modelling of interfacial transition zone at micro-scale, Cement Concr. Compos. (2019) 103383.
[55] O. Lloberas-Valls, D. Rixen, A. Simone, L. Sluys, On micro-to-macro connections in domain decomposition multiscale methods, Comput. Methods Appl. Mech. Eng. 225 (2012) 177–196.
[56] T.J.R. Hughes, G.R. Feijóo, L. Mazzei, J.-B. Quincy, The variational multiscale method—a paradigm for computational mechanics, Comput. Methods Appl. Mech. Eng. 166 (1) (1998) 3–24.
[57] H. Zhang, B. Šavija, S.C. Figueiredo, E. Schlangen, Experimentally validated multi-scale modelling scheme of deformation and fracture of cement paste, Cement Concr. Res. 102 (2017) 175–186.
[58] H. Zhang, B. Šavija, Y. Xu, E. Schlangen, Size effect on splitting strength of hardened cement paste: experimental and numerical study, Cement Concr. Compos. 94 (2018) 264–276.
[59] Z.P. Bažant, Size effect, Int. J. Solid Struct. 37 (1) (2000) 69–80.
[60] A. Carpinteri, S. Puzzi, Fractals, Statistics and Size-Scale Effects on Concrete Strength, Fracture Mechanics of Concrete Structures, 2007, pp. 31–37.
[61] Z. Qian, E.J. Garboczi, G. Ye, E. Schlangen, Anm: a geometrical model for the composite structure of mortar and concrete using real-shape particles, Mater. Struct. 49 (1) (2016) 149–158.
[62] H. Zhang, B. Šavija, E. Schlangen, Towards understanding stochastic fracture performance of cement paste at micro length scale based on numerical simulation, Construct. Build. Mater. 183 (2018) 189–201.
[63] H. Zhang, Y. Xu, Y. Gan, Z. Chang, E. Schlangen, B. Šavija, Combined experimental and numerical study of uniaxial compression failure of hardened cement paste at micrometre length scale, Cement Concr. Res. 126 (2019) 105925.
[64] H. Wong, M. Head, N. Buenfeld, Pore segmentation of cement-based materials from backscattered electron images, Cement Concr. Res. 36 (6) (2006) 1083–1090.
[65] A.M. Neville, Properties of Concrete, Pearson Education India, 1963.
[66] C. Du, L. Sun, S. Jiang, Z. Ying, Numerical simulation of aggregate shapes of three-dimensional concrete and its applications, J. Aero. Eng. 26 (3) (2013) 515–527.
[67] E.J.J.C. Garboczi, Three-dimensional mathematical analysis of particle shape using X-ray tomography and spherical harmonics: application to aggregates used in concrete, Cement Concr. Res. 32 (10) (2002) 1621–1638.
[68] M. Grigoriu, E. Garboczi, C.J.P.T. Kafali, Spherical harmonic-based random fields for aggregates used in concrete, Powder Technol. 166 (3) (2006) 123–138.
[69] X. Liu, E. Garboczi, M. Grigoriu, Y. Lu, S.T.J.P.T. Erdoğan, Spherical harmonic-based random fields based on real particle 3D data: improved numerical algorithm and quantitative comparison to real particles 207 (1–3) (2011) 78–86.
[70] Z. Qian, G. Ye, E. Schlangen, K. van Breugel, 3D lattice fracture model: application to cement paste at microscale, Key Eng. Mater. (2011) 65–68. Trans Tech Publ.
[71] B. Šavija, D. Liu, G. Smith, K.R. Hallam, E. Schlangen, P.E. Flewitt, Experimentally informed multi-scale modelling of mechanical properties of quasi-brittle nuclear graphite, Eng. Fract. Mech. 153 (2016) 360–377.
[72] G. Lilliu, 3D Analysis of Fracture Processes in Concrete, Delft University of Technology, Delft, The Netherlands, 2007.
[73] M. Yip, J. Mohle, J. Bolander, Automated modeling of three-dimensional structural components using irregular lattices, Comput. Aided Civ. Infrastruct. Eng. 20 (6) (2005) 393–407.
[74] A. Vervuurt, E. Schlangen, J.G. Van Mier, Tensile cracking in concrete and sandstone: Part 1—basic instruments, Mater. Struct. 29 (1) (1996) 9–18.
[75] I. Gitman, H. Askes, L. Sluys, Representative volume: existence and size determination, Eng. Fract. Mech. 74 (16) (2007) 2518–2534.
[76] L.-Y. Lv, H. Zhang, E. Schlangen, Z. Yang, F. Xing, Experimental and numerical study of crack behaviour for capsule-based self-healing cementitious materials, Construct. Build. Mater. 156 (2017) 219–229.
[77] B. Šavija, J. Pacheco, E. Schlangen, Lattice modeling of chloride diffusion in sound and cracked concrete, Cement Concr. Compos. 42 (2013) 30–40.
[78] H. Zhang, B. Šavija, M. Luković, E. Schlangen, Experimentally informed micromechanical modelling of cement paste: an approach coupling X-ray

computed tomography and statistical nanoindentation, Compos. B Eng. 157 (2019) 109–122.
[79] M. Hassanzadeh, Fracture mechanical properties of rocks and mortar/rock interfaces, MRS Online Proc. Library Archiv. 370 (1994).
[80] Z.P. Bažant, S.-D. Pang, Activation energy based extreme value statistics and size effect in brittle and quasibrittle fracture, J. Mech. Phys. Solid. 55 (1) (2007) 91–131.
[81] E. Schlangen, Experimental and Numerical Analysis of Fracture Processes in Concrete, Delft University of Technology, 1993.
[82] J. Eliáš, Generalization of load–unload and force-release sequentially linear methods, Int. J. Damage Mech. 24 (2) (2015) 279–293.
[83] J. Eliáš, P. Frantík, M. Vořechovský, Improved sequentially linear solution procedure, Eng. Fract. Mech. 77 (12) (2010) 2263–2276.
[84] Y. Gan, H. Zhang, B. Šavija, E. Schlangen, K. van Breugel, Micro-cantilever testing of cementitious materials under various loading conditions, in: Proceedings of the 10th International Conference on Fracture Mechanics of Concrete and Concrete Structures, 2019.